

Target Detection in Single- and Multiple-View Through-the-Wall Radar Imaging

Christian Debes, *Student Member*, Moeness G. Amin, *Fellow, IEEE*, and Abdelhak M. Zoubir, *Fellow, IEEE*

Abstract—A detector of targets behind walls and in enclosed structures is presented. The detector is applied to through-the-wall radar images obtained by wideband delay and sum beamforming. We consider the detection problem using single- and multiple-view imaging. The statistics of noise, clutter, and target images are examined and formulated using sample scenes. The effects of wall parameter errors on the image statistics are shown. An iterative detection scheme, which adapts itself to the image statistics, is presented. The proposed detection schemes are evaluated using real data.

Index Terms—Detection theory, radar imaging, through the wall (TTW).

I. INTRODUCTION

THROUGH-THE-WALL (TTW) radar imaging is an emerging technology, permitting seeing through visually opaque materials such as walls. It has numerous civilian, law-enforcement, and military applications. It is a highly desirable tool in, for example, police and firefighter missions or search and rescue operations in natural disasters [1]–[5]. In all these applications, it is the ultimate aim to use radio-frequency (RF) emission and reception to gain vision into scenes which, otherwise, are nonaccessible physically, optically, acoustically, or thermally.

Automatic detection of humans and objects of interest, e.g., concealed weapons or explosive material, is of high practical interest, which is fundamental to follow-on tasks of target classification and tracking, image interpretation, and understanding. Little work thus far has been done in applying the principles of detection theory to the special characteristics of TTW and indoor radar images. The target statistics in the image domain depends, among other things, on the target electric properties, size, shape, and surroundings. With several possible indoor targets such as human, furniture, and appliances, as well as the influence of wall impairing and multipath propagation effects, robust detection in which the detector adapts itself to the changing characteristics of the data is important.

In this paper, we present strategies for target detection in TTW radar imaging based on a classical detection theory [6].

Manuscript received May 14, 2008; revised September 24, 2008 and December 4, 2008. Current version published April 24, 2009. The work of M. G. Amin was supported in part by the Office of Naval Research under Grant N00014-07-1-0043.

C. Debes and A. M. Zoubir are with the Signal Processing Group, Institute of Telecommunications, Darmstadt University of Technology, 64289 Darmstadt, Germany (e-mail: cdebes@ieee.org; zoubir@ieee.org).

M. G. Amin is with the Center for Advanced Communications and the Department of Electrical and Computer Engineering, Villanova University, Villanova, PA 19085 USA (e-mail: amin@ieee.org).

Color versions of one or more of the figures in this paper are available online at <http://ieeexplore.ieee.org>.

Digital Object Identifier 10.1109/TGRS.2009.2013460

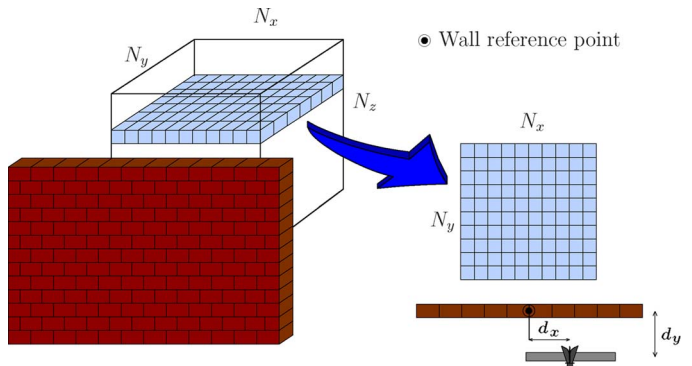


Fig. 1. Acquiring a B-Scan image from a 3-D scene.

The scene image is generated using wideband synthetic aperture beamforming. Multiviewing operations, in which different images of the same scene using different positions of the imaging system, are considered.

Section II provides a problem formulation and derives the likelihood ratio test (LRT) when observing the scene of interest from an arbitrary number of vantage points. In Section III, we examine the statistics of typical TTW radar images and find appropriate probability density functions for modeling noise and target returns. The effect of the wall, represented by its thickness and dielectric constant, is discussed in Section IV. Section V provides a robust iterative detection scheme for targets behind walls under unknown image statistics. Validation of our proposed detector with experimental data is provided in Section VI.

II. DETECTION SCHEMES FOR SINGLE- AND MULTIPLE-VIEWING SCENARIOS

A. Imaging From Single and Multiple Views

We consider the scenario shown in Fig. 1. A 3-D scene of interest (a cuboid of size $N_x \times N_y \times N_z$) is located behind a concrete wall, where N_x , N_y , and N_z represent the number of pixels in cross-range, range, and height, respectively. The scene is illuminated by a TTW radar system placed at the other side of the wall from d_x in horizontal distance and d_y standoff distance with respect to a wall reference point. The 2-D B-Scan images (downrange versus cross-range) are obtained by considering a particular height of interest.

As shown in Fig. 2, several setups are possible when acquiring the B-Scan images of size $N_x \times N_y$ from multiple vantage points. With access to one side of the building only, a set of M radar system positions can be considered along the same wall, shifted by $d_x^{1,m}$, $m = 1, \dots, M$ in horizontal distance and $d_y^{1,m}$, $m = 1, \dots, M$ in standoff distance with

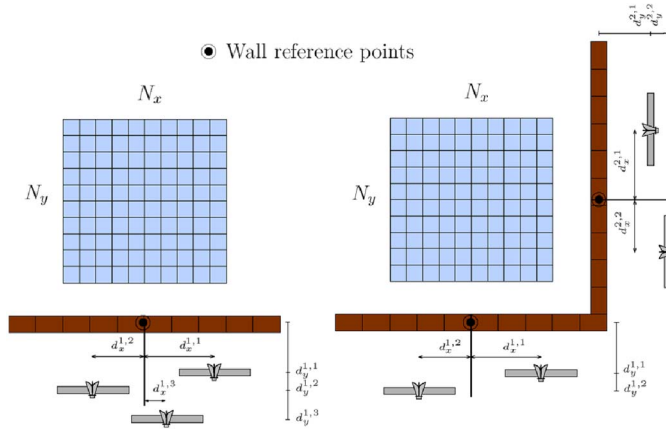


Fig. 2. Possible multiple-view scenarios.

respect to the center point, where m denotes the m th TTW radar system position. If access to p walls is possible [7], [8], the radar system can be placed facing different walls—again with arbitrary horizontal and standoff distances from the respective center points $d_x^{1,m}, \dots, d_x^{p,m}$ and $d_y^{1,m}, \dots, d_y^{p,m}$, $m = 1, \dots, M$, respectively.

Fusing the images from multiple vantage points is performed through translation and rotation operations such that the individual coordinate systems are aligned to a single reference coordinate system. The details of aligning TTW radar images have been presented in [9]. In the sequel, we assume that the set of the TTW radar images $\{X_m(i, j)\}_{m=1}^M$ have already been aligned and image registration has been performed.

B. Simple Thresholding Scheme

Consider M TTW radar images of the same scene obtained from multiple views. It is the aim of the detection scheme to process the images in such a way that information of the presence of targets and their locations becomes apparent.

We note that $X_m(i, j)$ assumes normalized values by scaling, with respect to the largest image value. Further, we only consider the absolute value of the complex array response, such that $X_m(i, j) \in [0, 1]$, where (i, j) represents the pixel position with i and j denoting the range and cross-range indices, respectively. A simple and intuitive way to perform detection is to binarize each TTW radar image for $m = 1, \dots, M$, $i = 1, \dots, N_x$ and $j = 1, \dots, N_y$ as

$$X_m^B(i, j) = \begin{cases} 1, & X_m(i, j) > \kappa \\ 0, & X_m(i, j) \leq \kappa \end{cases} \quad (1)$$

where κ is the image threshold. The individual images can be fused by applying, for example, a simple pixelwise multiplication in order to obtain a single reference image [9]

$$F^A(i, j) = \prod_{m=1}^M X_m^B(i, j) \quad (2)$$

where M is the total number of TTW radar images available for detection. The advantage of the pixelwise multiplication scheme is the reduction of clutter in the resulting binary reference image $F^A(i, j)$. When illuminating the scene of interest

from multiple views, clutter assumes different RF signatures, whereas targets appear at the same location in all images, provided that they have a small physical cross-sectional area in the x - y plane and are visible from all views. Applying (2), a pixel $F^A(i_0, j_0)$ is said to correspond to a target if and only if a strong reflection at location (i_0, j_0) is observed in each radar image. Strong reflections, which can only be observed in one or a few TTW radar images, are attributed to clutter and will be mitigated by the multiplication operation. The disadvantages of the pixelwise multiplication scheme are given as follows.

- 1) Choosing a “good” threshold κ is a nontrivial task.
- 2) When considering image formation from multiple views, a target might only be visible from a few vantage points and is overshadowed, partially or completely, by other targets, e.g., due to masking. Pixelwise multiplication is only effective when targets are visible from all vantage points and have a small physical cross-sectional area in the x - y plane.

C. Neyman–Pearson Test

An alternative to the simple thresholding scheme, proposed in [9] and presented in Section II-B, is to formulate a hypothesis test and to derive a Neyman–Pearson test [6]. We define the pixelwise null and alternative hypotheses as

$$\begin{aligned} H_0 &: \text{no target present at pixel } (i, j) \\ H_1 &: \text{target present at pixel } (i, j). \end{aligned}$$

Assuming the data to be independent and identically distributed, the LRT is given by

$$LR(i, j) = \prod_{m=1}^M \frac{p(X_m(i, j)|H_1)}{p(X_m(i, j)|H_0)} \stackrel{H_1}{\leq} \gamma \quad (3)$$

where $p(X_m(i, j)|H_0)$ and $p(X_m(i, j)|H_1)$ are the conditional probability density functions (pdfs) of the acquired image, given the null and alternative hypotheses, respectively. The parameter γ is the LRT threshold which maximizes the probability of detection while controlling the probability of false alarm. Given the image statistics $p(X_m(i, j)|H_0)$ and $p(X_m(i, j)|H_1)$ and the threshold γ , the fused binary image can easily be calculated as

$$F^{\text{NP}}(i, j) = \begin{cases} 1, & LR(i, j) > \gamma \\ 0, & LR(i, j) \leq \gamma. \end{cases} \quad (4)$$

Using the Neyman–Pearson theorem [6], the false-alarm rate can be fixed by evaluating

$$\alpha = \int_{\gamma}^{\infty} f_L(L|H_0) dL \quad (5)$$

where α and $f_L(L|H_0)$ are, respectively, the false-alarm rate (Type I error) and the distribution of the likelihood ratio under the null hypothesis.

The advantages of this detector compared with the thresholding scheme from Section II-B are as follows.

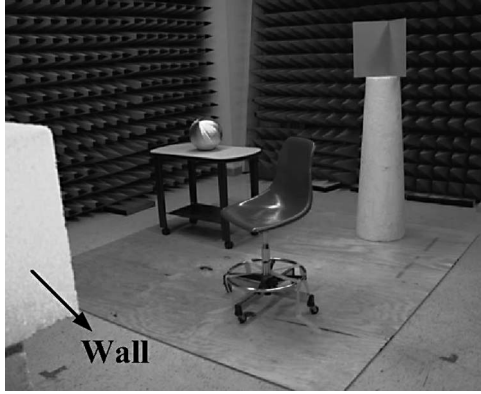


Fig. 3. Imaged indoor scene.

- 1) The statistics of the TTW radar images can be incorporated in the detection scheme by choosing appropriate conditional density functions $p(X_m(i, j)|H_0)$ and $p(X_m(i, j)|H_1)$.
- 2) There is a meaningful way to choose the threshold γ by considering an acceptable false-alarm rate.
- 3) A target, at location (i_0, j_0) , which is invisible or masked from one or few vantage points, may still appear in the fused image, given that the likelihood ratio in (3) is higher than γ . This requires a sufficiently likely reflection amplitude at (i_0, j_0) from a single view corresponding to one position of the imaging system. The same statement holds for targets with a large cross-sectional area, which are illuminated in a different way from each vantage point.

III. STATISTICAL PROPERTIES OF TTW RADAR IMAGES

When using the detector presented in Section II-C, the information about the image statistics, i.e., the conditional pdfs of the image pixels under the null and alternative hypotheses should be known. In the absence of this knowledge, one may resort to, for example, resampling techniques, such as the bootstrap, to extract this information [10]. This approach is being investigated but is not presented here. Instead, we proceed as described in the following. We consider the setup for a typical indoor scenario, shown in Fig. 3, consisting of a table with metal legs, a chair, a metal sphere, and a metal dihedral mounted on a high foam column. The last two items represent indoor symmetric objects and objects of corner reflection properties, respectively.

For imaging, a 57×57 element planar array has been synthesized by using a single horn antenna. The interelement spacing is 0.875 in. A stepped-frequency continuous-wave (CW) signal is used to illuminate the scene. The bandwidth is 2.4 GHz, with a center frequency of 1.9 GHz. Each image consists of 117×117 pixels with a resolution of 1.23 in. The targets occupy approximately 108 pixels (dihedral), 69 pixels (sphere), and 144 pixels (table legs). A wideband synthetic aperture beamformer is used to generate the radar image. We briefly present its fundamental equations, while referring to [9] for more details.

Let $\mathbf{x}_{tk} = (x_{tk}, y_{tk}, -d_y^{p,m})$ denote the k th transceiver location, with $d_y^{p,m}$ representing the standoff distance of the

m th receiver from the p th vantage point. A point target, located at $\mathbf{x}_p = (x_p, y_p, z_p)$, yields a complex amplitude $\mathbf{r}_{kl} = a(\mathbf{x}_p) \exp(-j\omega_l \tau_{kp})$ measured at the k th receiver. Here, $a(\mathbf{x}_p)$ is the reflectivity of the point target, ω_l denotes the l th frequency of the stepped-frequency CW signal, and τ_{kp} is the two-way signal propagation delay given by [9]

$$\tau_{kp} = 2 \cdot (l_{kp,air,1} + \sqrt{\epsilon} l_{kp,wall} + l_{kp,air,2})/c \quad (6)$$

where ϵ denotes the dielectric constant of the wall; c is the speed of light; and $l_{kp,air,1}$, $l_{kp,wall}$, and $l_{kp,air,2}$ represent the traveling distances of the electromagnetic wave before, through, and beyond the wall, respectively. The complex amplitude corresponding to an image voxel of interest $\mathbf{x}_q = (x_q, y_q, z_q)$ can then be calculated as

$$I(\mathbf{x}_q) = \sum_{l=1}^L \sum_{k=1}^K a(\mathbf{x}_p) \exp(-j\omega_L(\tau_{kp} - \tau_{kq})) \quad (7)$$

with L and K denoting the total number of radar frequency bins and array elements, respectively. Equation (7) considers monostatic data collection, where transmit–receive pairs are equal to the number of antenna elements. It is performed for all voxels in the 3-D scene of interest.

When focusing the array on various heights h in the 3-D scene image, different statistics can be obtained. In particular, we consider the following four cases with different clutters.

- 1) Case 1), $h = h_1(-2$ in). “No target”: We examine the image at the height between the dihedral and the metal sphere where no target is present, and only a small amount of clutter due to targets at other heights can be observed.
- 2) Case 2), $h = h_2(+7$ in). “Dihedral”: The image at the height of the dihedral is examined. At this height, no other targets are present, and only a small amount of clutter contributed by targets at other heights is expected.
- 3) Case 3), $h = h_3(-20.5$ in). “Table”: The image at the height of the table legs is examined. A medium amount of clutter is expected due to, for example, the metal sphere, the chair, and reflections from the ground. Note that the height at the top of the table legs is focused such that the chair leg is considered as clutter, not a target.
- 4) Case 4), $h = h_4(-15$ in). “Metal sphere”: The image at the height of the center of the metal sphere is examined. A large amount of clutter is expected, mainly due to the table legs.

The four resulting background-subtracted B-Scan images [11], which are obtained by scanning the indoor scene behind the solid concrete wall, are shown in Fig. 4.

The background subtraction has been performed by making use of reference or background data (here, a room without objects) and performing coherent subtraction. This reference data may be secured in long-term surveillance operations where new targets emerge over time. Targets of interest [e.g., the four table legs in Case 3) or the metal sphere in Case 4)] are

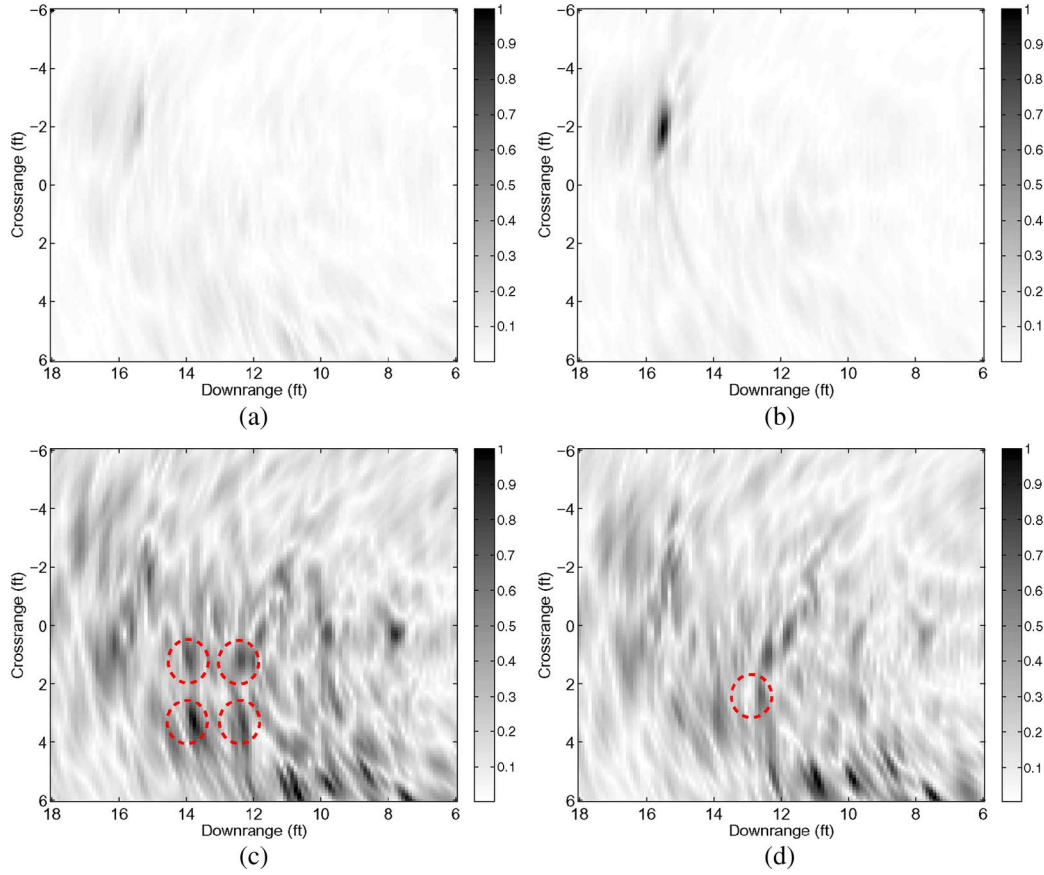


Fig. 4. B-Scan images. (a) Case 1), no target. (b) Case 2), metal dihedral. (c) Case 3), table legs. (d) Case 4), metal sphere.

indicated by red circles. Given the precise locations of these targets of interest in each of the aforementioned cases, the target image can be described as

$$T_h(i, j) = \begin{cases} 1, & \text{target present at height } h \text{ and location } (i, j) \\ 0, & \text{target absent at height } h \text{ and location } (i, j) \end{cases} \quad (8)$$

with $h \in \{h_1, \dots, h_4\}$, $i = 1, \dots, N_x$ and $j = 1, \dots, N_y$. Let $\{X_m^h(i, j)\}_{m=1}^M$ denote the total set of image values at height h . This set can be divided into a set of target samples \mathcal{T}_h and a set of noise samples \mathcal{N}_h

$$\mathcal{T}_h = \{X_m^h(i, j) | T_h(i, j) = 1\}_{m=1}^M \quad (9)$$

$$\mathcal{N}_h = \{X_m^h(i, j) | T_h(i, j) = 0\}_{m=1}^M. \quad (10)$$

The sets $\mathcal{T}_h, \mathcal{N}_h$ associated with the aforementioned experiment with $h = h_1, h_2, h_3, h_4$ are now used to evaluate the statistics of noise and target data in background-subtracted TTW radar images. For simplicity, we use two vantage points ($M = 2$), one from the front wall and one from the side wall, to form the two sets of noise and target samples. The resulting estimated probability density functions, which have been obtained using kernel density estimation [12], are shown in Fig. 5. In the kernel density estimation, a pdf is estimated by placing a kernel, e.g., a Gaussian kernel, at each data point. The estimate of the pdf is then obtained by summation over all kernels and subsequent

normalization. This method is particularly effective when only a few data points are available, which is the case for the target data in the images shown earlier.

It is shown in Fig. 5 that the image statistics vary significantly from one case to another. In Cases 1) and 2), the amount of noise and clutter is relatively small; their pdf is well separated from the target data pdf, which improves detection. On the other hand, in Cases 3) and 4), the amount of noise and clutter is relatively large, yielding strong overlapping pdfs, which complicates detection. It can be observed that, in Case 4), approximately 12% of the strongest reflections obtained are not due to targets but rather due to clutter.

The pdfs, shown in Fig. 5, strongly suggest modeling the noise as a truncated Rayleigh distribution. The target pdf is highly dependent on the target size, material, and shape, which makes it difficult to draw general conclusions on its image statistics. From the experimental data, however, the target image pdf appears to consistently follow a truncated Gaussian distribution. Both the noise Rayleigh and the target Gaussian pdfs have also been shown to be valid assumptions in extensive experiments we have conducted using different targets. These experiments maintained the same semicontrolled lab environment and included various room items, such as chairs, tables, and file cabinets, as well as metal objects, such as cylinders, with different shapes. When evaluating the pdf, all these objects were illuminated by the same array aperture. It is noted that truncated Gaussian pdfs have also been used in [13] for describing the target distribution in multiple-location SAR/ISAR image fusion.

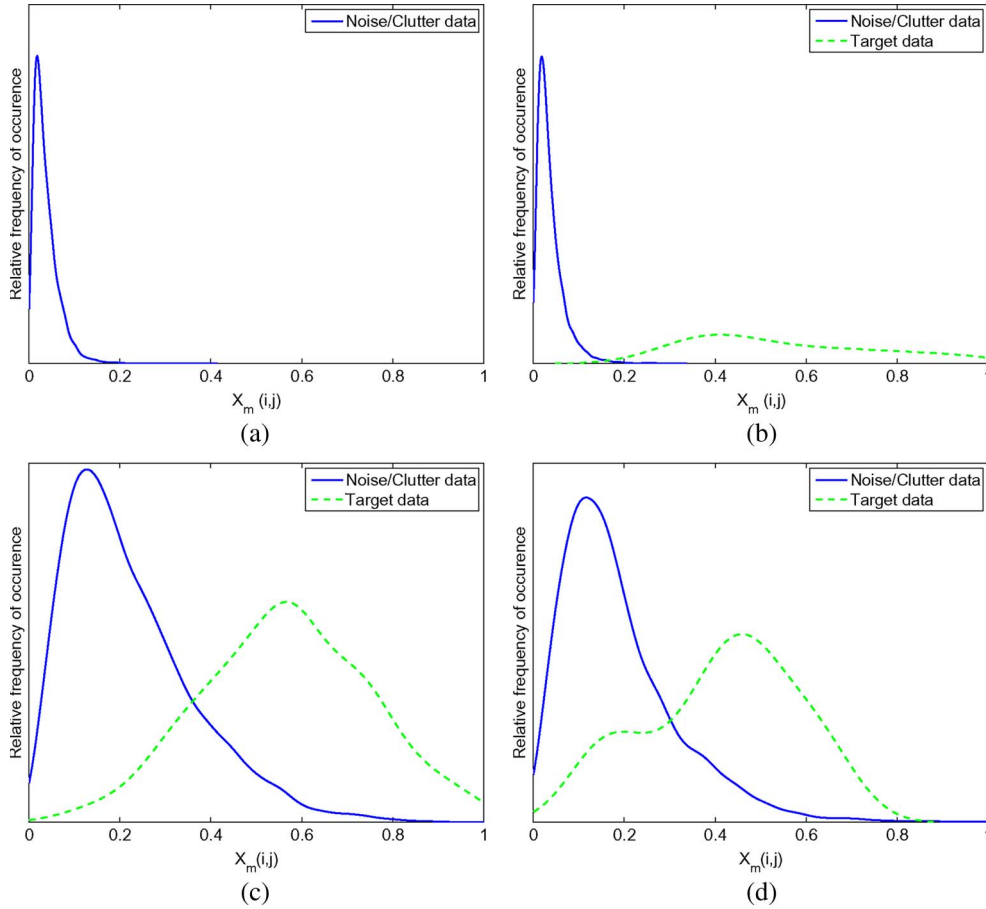


Fig. 5. Estimated image statistics. (a) Case 1). (b) Case 2). (c) Case 3). (d) Case 4).

The assumed pdfs under the null and alternative hypotheses are then

$$p(X_m(i, j)|H_0) = \mathcal{S} \left(\frac{X_m(i, j)}{\sigma_0^2} \cdot e^{-\frac{X_m^2(i, j)}{2\sigma_0^2}} \right) \quad (11)$$

$$p(X_m(i, j)|H_1) = \mathcal{S} \left(\frac{1}{\sqrt{2\pi}\sigma_1} \cdot e^{-\frac{(X_m(i, j) - \mu)^2}{2\sigma_1^2}} \right) \quad (12)$$

where $\mathcal{S}(\cdot)$ is an operation for truncation and normalization such that

$$\int_{-\infty}^{\infty} p(\varphi|H_0)d\varphi = \int_0^1 p(\varphi|H_0)d\varphi = 1$$

$$\int_{-\infty}^{\infty} p(\varphi|H_1)d\varphi = \int_0^1 p(\varphi|H_1)d\varphi = 1.$$

Accordingly

$$p(X_m(i, j)|H_0) = \left(1 - e^{-1/2\sigma_0^2}\right)^{-1} \cdot \frac{X_m(i, j)}{\sigma_0^2} \cdot e^{-\frac{X_m^2(i, j)}{2\sigma_0^2}} \quad (13)$$

$$p(X_m(i, j)|H_1) = \frac{1}{\sqrt{2\pi}\sigma_1} \left(\operatorname{erf} \left(\frac{1 - \mu}{\sqrt{2}\sigma_1} \right) - \operatorname{erf} \left(\frac{-\mu}{\sqrt{2}\sigma_1} \right) \right)^{-1} \cdot e^{-\frac{(X_m(i, j) - \mu)^2}{2\sigma_1^2}} \quad (14)$$

with $m = 1, \dots, M, i = 1, \dots, N_x$, and $j = 1, \dots, N_y$. In (14), $\operatorname{erf}(\cdot)$ represents the error function. Given $p(X_m(i, j)|H_0)$ and $p(X_m(i, j)|H_1)$, the LRT from (3) can be written as

$$LR(i, j) = \lambda^M \prod_{m=1}^M \frac{1}{X_m(i, j)} e^{-\left(\frac{X_m(i, j) - \mu}{2\sigma_1^2}\right)^2 + \frac{X_m^2(i, j)}{2\sigma_0^2}} \underset{H_0}{\overset{H_1}{\leq}} \gamma \quad (15)$$

with $m = 1, \dots, M, i = 1, \dots, N_x$, and $j = 1, \dots, N_y$, where

$$\lambda = \frac{\sigma_0^2 \left(1 - e^{-1/2\sigma_0^2}\right)}{\sqrt{2\pi}\sigma_1 \left(\operatorname{erf} \left(\frac{1 - \mu}{\sqrt{2}\sigma_1} \right) - \operatorname{erf} \left(\frac{-\mu}{\sqrt{2}\sigma_1} \right) \right)}. \quad (16)$$

Since the noise and target pdfs can be, respectively, modeled as a truncated Rayleigh and a truncated Gaussian pdf, one can obtain the maximum-likelihood estimates of the respective parameters $\hat{\sigma}_0, \hat{\mu}$, and $\hat{\sigma}_1$ as

$$\hat{\mu} = \arg \max_{\mu} \prod_w i = 1^{N_x} \prod_{j=1}^{N_y} \mathcal{S} \left(\frac{1}{\sqrt{2\pi}\sigma_1} \cdot e^{-\frac{(X_m(i, j) - \mu)^2}{2\sigma_1^2}} \right) \quad (17)$$

$$\hat{\sigma}_1 = \operatorname{argmax}_{\sigma_1} \prod_{i=1}^{N_x} \prod_{j=1}^{N_y} \mathcal{S} \left(\frac{1}{\sqrt{2\pi}\sigma_1} \cdot e^{-\frac{(X_m(i, j) - \mu)^2}{2\sigma_1^2}} \right) \quad (18)$$

$$\hat{\sigma}_0 = \operatorname{argmax}_{\sigma_0} \prod_{i=1}^{N_x} \prod_{j=1}^{N_y} \mathcal{S} \left(\frac{X_m(i, j)}{\sigma_0^2} \cdot e^{-\frac{X_m^2(i, j)}{2\sigma_0^2}} \right). \quad (19)$$

TABLE I
ML ESTIMATES OF THE NOISE AND TARGET PARAMETERS
UNDER NONTRUNCATED AND TRUNCATED PDFS

Height	$\hat{\sigma}_0$	$\hat{\sigma}_0^{NT}$	$\hat{\mu}$	$\hat{\mu}^{NT}$	$\hat{\sigma}_1$	$\hat{\sigma}_1^{NT}$
h_1	0.08	0.08	–	–	–	–
h_2	0.09	0.09	0.57	0.58	0.19	0.21
h_3	0.19	0.19	0.53	0.53	0.18	0.18
h_4	0.16	0.16	0.42	0.41	0.16	0.16

Note that, due to the truncating operation $\mathcal{S}(\cdot)$, a closed-form solution for $\hat{\sigma}_0$, $\hat{\mu}$, and $\hat{\sigma}_1$ is not available. The estimates can be found numerically, e.g., using a hill-climbing algorithm to find the maximum of the likelihood function. However, as shown in Fig. 5, the pdfs only have little impact outside the interval $[0, 1]$, indicating that the estimates from (17)–(19), which are computationally expensive, can be replaced by the maximum-likelihood estimates given the nontruncated Gaussian and Rayleigh pdfs

$$\hat{\mu}^{NT} = \frac{1}{N_x \cdot N_y} \sum_{i=1}^{N_x} \sum_{j=1}^{N_y} X_m(i, j) \quad (20)$$

$$\hat{\sigma}_1^{NT} = \sqrt{\frac{1}{N_x \cdot N_y} \sum_{i=1}^{N_x} \sum_{j=1}^{N_y} (X_m(i, j) - \mu^{NT})^2} \quad (21)$$

$$\hat{\sigma}_0^{NT} = \sqrt{\frac{1}{2N_x \cdot N_y} \sum_{i=1}^{N_x} \sum_{j=1}^{N_y} X_m^2(i, j)} \quad (22)$$

with $m = 1, \dots, M$, $i = 1, \dots, N_x$, and $j = 1, \dots, N_y$, where the superscript NT stands for nontruncated. In Table I, the maximum-likelihood estimates for the four considered cases are shown. It is clear that the estimates obtained using the nontruncated pdfs are close to those which are generated with the truncated pdfs. As shown by the results of Fig. 5, the image statistics may change dramatically, depending on the scene. Since detailed knowledge of the scene is unavailable in practice, the detection scheme needs to be robust against errors in the parameter values of the assumed pdfs.

It should also be noted that the conditional distributions depend on the image resolution, i.e., the array aperture and the bandwidth of the signal used to illuminate the scene. A high image resolution will lead to narrow pdfs, representing target and noise distributions. A low image resolution, on the other hand, yields blurring effects, leading to broader pdfs.

It is noted that background subtraction affects the statistics of targets, and thus, different conclusions have to be drawn when secondary data are not available.

IV. WALL EFFECTS

When acquiring the TTW radar images using, for example, the wideband beamformer presented in [11], it is assumed that the wall parameters, such as the wall thickness d and dielectric constant ϵ , are known. However, in practice, due to operation logistics and safety factors, these quantities are generally unknown or difficult to discern accurately. Accordingly, the

estimates \hat{d} and $\hat{\epsilon}$ are subject to errors. The effects of errors in the wall parameters on the TTW radar image and methods to accurately estimate these parameters have been treated in [14]–[17] and are not discussed in this paper. The two main effects in assuming the incorrect wall parameters $d \pm \Delta d$ and $\epsilon \pm \Delta \epsilon$ stem from the changes in the focusing delays when applying the wideband beamforming algorithm, i.e.,

- 1) target displacement (targets will be shifted away from their true positions);
- 2) target blurring (the targets will be out of focus, i.e., blurred).

When considering the detection approach from Section II-C based on the conditional pdfs $p(X_m(i, j)|H_0)$ and $p(X_m(i, j)|H_1)$, $m = 1, \dots, M$, $i = 1, \dots, N_x$, $j = 1, \dots, N_y$, a pure displacement of targets does not affect the distribution of target and noise samples. Blurring, however, will lead to a change of the pdfs' shape and can cause a problem for a detector, which relies on correct assumptions.

We demonstrate, in the following, the impact of wall parameter errors on the pdfs under the null and alternative hypotheses. As previously inferred, the noise and clutter samples are assumed to follow a truncated Rayleigh distribution, whereas target samples are assumed to follow a truncated Gaussian distribution.

For the “no-target” case [Case 1), Section III], the effect of wrong wall parameters $d \pm \Delta d$ and $\epsilon \pm \Delta \epsilon$ is shown in Fig. 6(a). The true wall parameters for the experiment are $d = 5.625$ in and $\epsilon = 7.66$ (indicated by a black arrow). shows the change in the maximum-likelihood estimate of the scale parameter $\hat{\sigma}_0$ of the Rayleigh distribution. It can be seen that when $\Delta \epsilon > 0$ and/or $\Delta d > 0$, the scale parameter increases, implying that the LRT threshold γ will mistakenly be chosen smaller. In this case, the resulting false-alarm rate will be higher than the desired α , based on (5). When $\Delta \epsilon < 0$ and/or $\Delta d < 0$, the scale parameter decreases, yielding a smaller false-alarm rate than α . Both cases are undesirable. Similar results can be obtained for the “target” case [Case 2) in Section III], which is shown in Fig. 6(b). The sensitivity of the aforementioned detector to wall parameter ambiguities is considered a drawback, and a practical detection scheme for TTW radar images should be devised to properly cope with these effects.

Apart from image degradations due to incorrect wall parameters, one should also note that, due to multiple reflections inside the wall, “ghost targets” are likely to appear. These “ghost targets” may have similar statistics to those of real targets; however, are displaced in the image. This effect is shown in Fig. 4.

V. ITERATIVE DETECTION APPROACH

A shortcoming of the Neyman–Pearson test presented in Section II-C is that the statistics of the TTW radar images of interest need to be known, i.e., one assumes the conditional density functions $p(X_m(i, j)|H_1)$ and $p(X_m(i, j)|H_0)$ to be available for $m = 1, \dots, M$, $i = 1, \dots, N_x$ and $j = 1, \dots, N_y$. This information is target and scene dependent, which is unknown in practice, and, as such, the proposed detector may be inapplicable. We present an extension of the aforementioned detector, which iteratively adapts the parameters of the Neyman–Pearson test to the TTW radar image statistics.

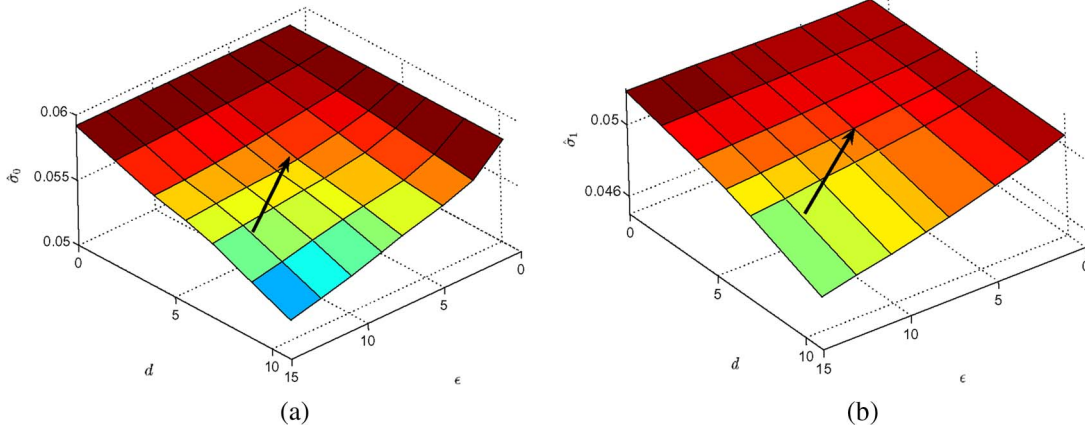


Fig. 6. Effect of wall parameter errors on the pdfs of H_0 and H_1 . (a) Effect on $p(X_m(i,j)|H_0)$ measured by σ_0 . (b) Effect on $p(X_m(i,j)|H_1)$ measured by σ_1 .

Initial values of the parameters $\hat{\theta}^{H_0,I} = [\hat{\theta}_1^{H_0,I}, \dots, \hat{\theta}_P^{H_0,I}]^T$ and $\hat{\theta}^{H_1,I} = [\hat{\theta}_1^{H_1,I}, \dots, \hat{\theta}_Q^{H_1,I}]^T$ are assumed, describing the density functions under the null and alternative hypotheses, as well as the desirable false-alarm rate α to be achieved. The Neyman–Pearson test can be applied to obtain an initial estimate of the fused binary image $F^{NP,I}(i,j)$, $i = 1, \dots, N_x$, $j = 1, \dots, N_y$, yielding the first rough indication of target locations. It is expected that, due to the pixelwise detection scheme, $F^{NP,I}(i,j)$, $i = 1, \dots, N_x$, $j = 1, \dots, N_y$ will generally be subject to outliers, i.e., isolated pixels or small regions of pixels whose intensity is higher than the average intensity of their surrounding. These outliers occur due to Type I errors. Using a preprocessing scheme, such as 2-D order-statistics filters [18], a cleaned binary reference image $F_C^{NP,I}(i,j)$, $i = 1, \dots, N_x$, $j = 1, \dots, N_y$ can be obtained. Given this first indication of target locations, one can now divide the total data set $\{X_m(i,j)\}_{m=1}^M$, $i = 1, \dots, N_x$, $j = 1, \dots, N_y$ into the sets

$$\mathcal{T} = \left\{ X_m(i,j) | F_C^{NP,I}(i,j) = 1 \right\}_{m=1}^M \quad (23)$$

$$\mathcal{N} = \left\{ X_m(i,j) | F_C^{NP,I}(i,j) = 0 \right\}_{m=1}^M \quad (24)$$

with $i = 1, \dots, N_x$, $j = 1, \dots, N_y$. \mathcal{T} and \mathcal{N} represent the set of target and the set of noise/clutter samples, respectively. Assuming these sets to be representative for the target and noise/clutter distributions, the maximum-likelihood estimates can be obtained, as discussed in Section III and given by (17)–(22)

$$\hat{\theta}^{H_0} = \arg \max_{\underline{\theta}} L(\underline{\theta}; \underline{n}) = \arg \max_{\underline{\theta}} \prod_{k=1}^{N_n} p(\theta; n(k), H_0) \quad (25)$$

$$\hat{\theta}^{H_1} = \arg \max_{\underline{\theta}} L(\underline{\theta}; \underline{t}) = \arg \max_{\underline{\theta}} \prod_{k=1}^{N_n} p(\theta; t(k), H_1) \quad (26)$$

where \underline{n} and \underline{t} are vectors containing all elements from \mathcal{N} and \mathcal{T} , respectively. The new estimates $\hat{\theta}^{H_0}$ and $\hat{\theta}^{H_1}$ can now be forwarded to the detection scheme to estimate a revised fused image $F^{NP,I}(i,j)$, $i = 1, \dots, N_x$, $j = 1, \dots, N_y$, which

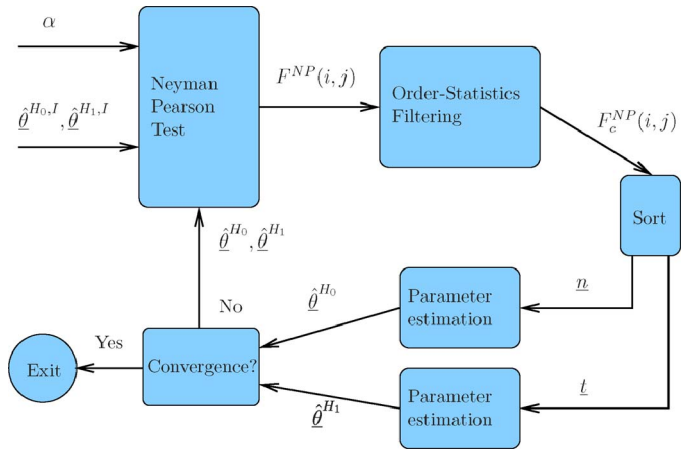


Fig. 7. Block diagram representation of the iterative detection approach.

can, in turn, be used to obtain the newly revised estimates $\hat{\theta}^{H_0}$ and $\hat{\theta}^{H_1}$. This procedure is continued until convergence is achieved, which is indicated by a vanishing difference between the current and the previous parameter estimates or the current and the previous fused image. A block diagram of the iterative scheme is shown in Fig. 7.

Considering the initial parameter estimates of the aforementioned iterative technique, it is preferred to have the two assumed conditional density functions $p(X_m(i,j)|H_0)$ and $p(X_m(i,j)|H_1)$, $m = 1, \dots, M$, $i = 1, \dots, N_x$, $j = 1, \dots, N_y$ of considerable overlap. This will, in essence, lead to a rather small image threshold $0 \leq \kappa \leq 1$, allowing a large number of target samples in $F^{NP,I}(i,j)$ to be generated and used to obtain $\hat{\theta}^{H_1}$. Weakly overlapping or nonoverlapping pdfs will yield a small number of target samples in $F^{NP,I}(i,j)$, $i = 1, \dots, N_x$, $j = 1, \dots, N_y$ and, applying the 2-D order statistic filter (e.g., a 2-D median filter for outlier removal) used to obtain $F_C^{NP,I}(i,j)$, $i = 1, \dots, N_x$, $j = 1, \dots, N_y$, will lead to an unreliable estimate $\hat{\theta}^{H_0}$.

VI. EXPERIMENTAL RESULTS

In order to evaluate the performance of the Neyman–Pearson test and the proposed iterative detection scheme, we consider

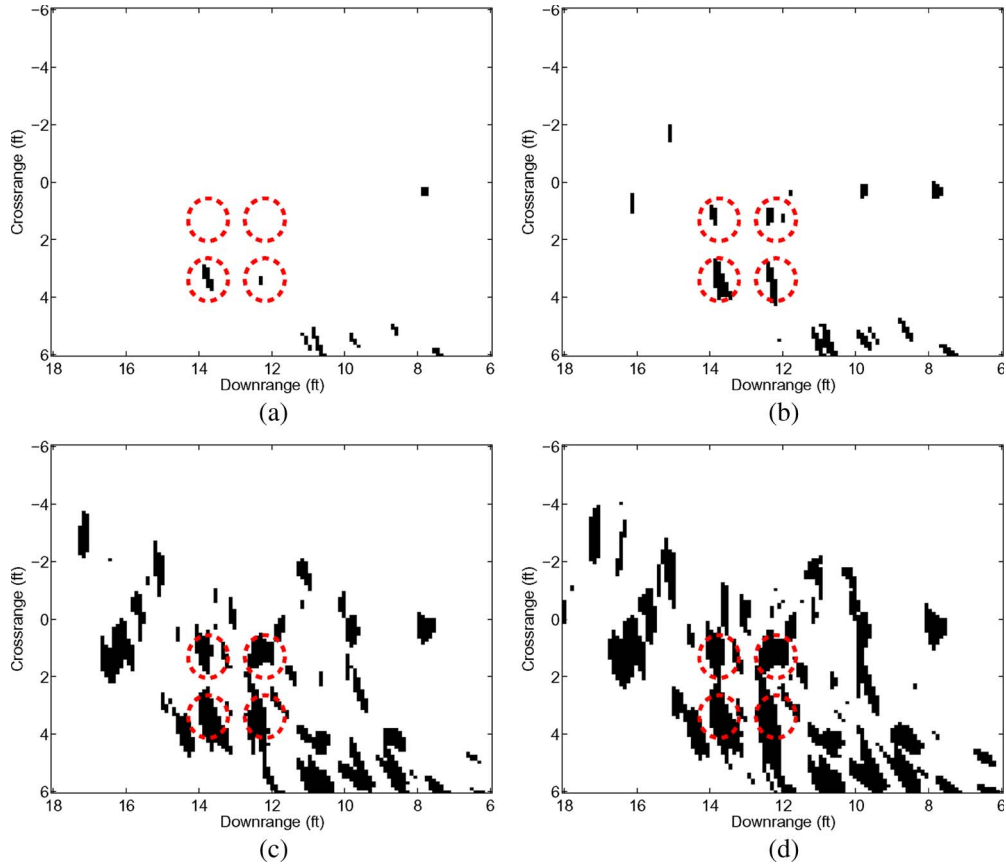


Fig. 8. Detection results for various false-alarm rates. Circles indicate the true position of the table legs. (a) $\alpha = 0.001$. (b) $\alpha = 0.01$. (c) $\alpha = 0.05$. (d) $\alpha = 0.1$.

the problem of detecting and estimating the location of the four table legs, as has already been presented in Section III. We consider single- and multiple-view imaging using background-subtracted TTW radar images.

In addition to a comparison between the standard Neyman–Pearson test and the proposed iterative detection scheme, we also compare the proposed detector to the order statistic constant-false alarm rate (OSCFAR) detector introduced by Rohling [19], which has also been derived under the assumption of Rayleigh distributed clutter. As suggested by Rohling, the 75th percentile has been used to obtain the image threshold.

The image acquisition is performed using a wideband synthetic aperture TTW radar system. We consider single-polarization arrays to be used, although the work can be extended to dual-polarization arrays [20]. The experiment was set up in the Radar Imaging Lab at Villanova University, Villanova, PA. An Agilent network analyzer, model ENA 5071B, has been chosen for synthesizing a stepped-frequency CW signal (801×3 MHz frequency steps, covering the 0.7–3.1-GHz band) and collecting the data. A horn antenna, model ETS-Lindgren 3164-04, has been used to synthesize a 57×57 element planar array (element distance is 0.875 in). A concrete wall with thickness $d = 5.625$ in and dielectric constant $\epsilon = 7.66$ is placed in front of the TTW radar system with stand-off distances $d_y = 40$ in and $d_x = 0$ in. In order to perform multiple-view imaging, the objects are mounted on a turntable and have been turned by 90° to emulate imaging from a side wall.

A. Single-View Imaging, Standard Approach

When considering a single vantage point, the LRT reduces to

$$LR(i, j) = \lambda \frac{1}{X_1(i, j)} e^{-\left(\frac{X_1(i, j) - \mu}{2\sigma_1^2}\right)^2 + \frac{X_1^2(i, j)}{2\sigma_0^2}} \underset{H_0}{\overset{H_1}{\leq}} \gamma \quad (27)$$

with $i = 1, \dots, N_x, j = 1, \dots, N_y$, where λ is defined in (16). It is easier to evaluate the log LRT (LLRT), which can be written as

$$LLR(i, j) = \ln(\lambda) - \ln(X_1(i, j)) - \left(\frac{X_1(i, j) - \mu}{2\sigma_1^2}\right)^2 + \frac{X_1(i, j)^2}{2\sigma_0^2} \underset{H_0}{\overset{H_1}{\leq}} \ln(\gamma) \quad (28)$$

with $i = 1, \dots, N_x, j = 1, \dots, N_y$. Using a desired false-alarm rate α , the parameter γ can be calculated, as per (5). The maximum-likelihood estimates for μ , σ_0 , and σ_1 are obtained from the statistical evaluation of the true target and noise/clutter samples, as described in Section III ($\hat{\mu} = 0.53, \hat{\sigma}_0 = 0.19, \hat{\sigma}_1 = 0.18$). For the case considered, the wall parameters d and ϵ are assumed to be known.

In Fig. 8, the resulting binary images for various false-alarm rates ($\alpha = 0.001, 0.01, 0.05$, and 0.1) are shown. The circles indicate the true position of the table legs [Case 3]. It is evident from this specific example that a false-alarm rate of at least 1% is needed in order to identify all four table legs. Further,

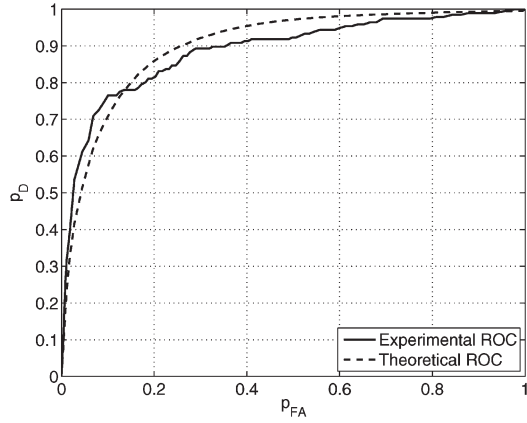


Fig. 9. ROC for single-view imaging.

a strong amount of clutter, even for small false-alarm rates, can be observed in all the images.

For a more objective measure of quality of the proposed method, the receiver operating characteristic (ROC) obtained from the experimental data is evaluated, representing the probability of detection p_D as a function of the probability of false alarm p_{FA} . This empirical ROC can be obtained by choosing various nominals p_{FA} and estimating the corresponding probability of detection p_D based on the true target locations and the estimated pdfs shown in Fig. 5. The empirical ROC is then compared with the theoretical ROC, derived using the likelihood ratio distributions $f_L(L|H_0)$ and $f_L(L|H_1)$, as well the relationships for p_{FA} and p_D

$$\begin{aligned} p_{FA} &= \int_{\gamma}^{\infty} f_L(L|H_0) dL \\ p_D &= 1 - \int_0^{\gamma} f_L(L|H_1) dL. \end{aligned} \quad (29)$$

Both ROC curves are shown in Fig. 9. It can be observed that the empirical ROC closely follows the theoretical ROC, which may suggest that the chosen pdfs under the null and alternative hypotheses reasonably match the estimated functions experimentally.

B. Single-View Imaging, Iterative Approach

One should note that the parameter estimates $\hat{\mu}$, $\hat{\sigma}_0$, and $\hat{\sigma}_1$, which were chosen for the Neyman–Pearson test, are the maximum-likelihood estimates, given the true target and noise/clutter data. In practice, these parameters are usually unknown.

In the following, we demonstrate the performance of the iterative detection scheme from Section V. To detect the location of the four table legs, the iterative detection scheme is applied using the following initial parameter estimates: $\hat{\mu}^0 = 0.3$, $\hat{\sigma}_0^0 = 0.1$, and $\hat{\sigma}_1^0 = 0.1$. Note that these initial parameters largely differ from the maximum-likelihood estimates obtained from the true target and noise/clutter data.

In Fig. 10, the resulting binary images of the proposed scheme obtained after 1–5 iterations are shown for a false-alarm rate $p_{FA} = 0.01$. In Fig. 10(a), the initial target indication image $F_C^{NP,I}(i, j)$, $i = 1, \dots, N_x$, $j = 1, \dots, N_y$ is shown. It can be seen that, due to the large errors introduced when

using a wrong distribution parameter set, the image threshold assumes a very low value such that the targets of interest cannot be detected (the actual false-alarm rate \tilde{p}_{FA} is $\approx 26\%$). After applying a 2-D order statistics filter (we chose a 5×5 2-D median filter for this purpose), a cleaned version $F_C^{NP,I}(i, j)$ is obtained, as shown in Fig. 10(b). Note that, due to the outlier removal, the false-alarm rate can already be decreased by 2%. When estimating the parameter set based on the first rough target and noise indication image $F_C^{NP,I}(i, j)$, $i = 1, \dots, N_x$, $j = 1, \dots, N_y$, the Neyman–Pearson test can be used to extract a revised binary image shown in Fig. 10(c). The four table legs, as indicated by circles, are now visible and separated from the clutter contributions (the actual false-alarm rate is $\approx 5\%$). In Fig. 10(d), the revised binary image is shown after five iterations, giving an even better visibility of the targets and approaching the desired false-alarm rate of 1%. However, we still note significant false detections, particularly in the bottom right part of the image. These false detections, which have similar intensity and structure of those of the targets, are most likely to be “ghost targets” stemming from multipath propagation effects.

Fig. 11 shows the detection result obtained when using the OSCFAR. It can be seen that the amount of clutter is higher compared with the end result of the iterative detection scheme. However, we note that the OSCFAR result could be used as an initialization step to improve the performance of the iterative detection scheme.

The convergence of the iterative detection scheme can be shown by observing the parameter estimates $\hat{\mu}$, $\hat{\sigma}_0$, and $\hat{\sigma}_1$; the empirical probability of false-alarm \tilde{p}_{FA} ; and the empirical probability of detection \tilde{p}_D versus the number of iterations. These plots are shown in Fig. 12(a) and (b). Convergence can be observed after 3–5 iterations. The parameter estimates obtained after convergence are close to the maximum-likelihood estimates; further, \tilde{p}_{FA} converges to the desired probability of false alarm.

C. Multiple-View Imaging

In addition to the presentation of the Neyman–Pearson test and the iterative detection scheme, we will now consider the scenario when the scene of interest is illuminated by $M = 2$ vantage points, rotated by 90° . In this case, the LRT can be written as

$$\begin{aligned} LR(i, j) &= \lambda^2 \frac{1}{X_1(i, j) \cdot X_2(i, j)} \\ &\cdot e^{-\left(\frac{X_1(i, j) - \mu}{2\sigma_1^2}\right)^2 + \frac{X_1^2(i, j)}{2\sigma_0^2} - \left(\frac{X_2(i, j) - \mu}{2\sigma_1^2}\right)^2 + \frac{X_2^2(i, j)}{2\sigma_0^2}} \frac{H_1}{H_0} \leq \gamma^2 \end{aligned} \quad (30)$$

with $i = 1, \dots, N_x$, $j = 1, \dots, N_y$, where λ is defined in (16). The LLRT, which is used for implementation purposes, can be written as

$$\begin{aligned} LLR(i, j) &= 2 \ln(\lambda) - \ln(X_1(i, j) \cdot X_2(i, j)) \\ &- \left(\frac{X_1(i, j) - \mu}{2\sigma_1^2}\right)^2 - \left(\frac{X_2(i, j) - \mu}{2\sigma_1^2}\right)^2 \\ &+ \frac{X_1(i, j)^2 + X_2(i, j)^2}{2\sigma_0^2} \frac{H_1}{H_0} \leq 2 \ln(\gamma) \end{aligned} \quad (31)$$

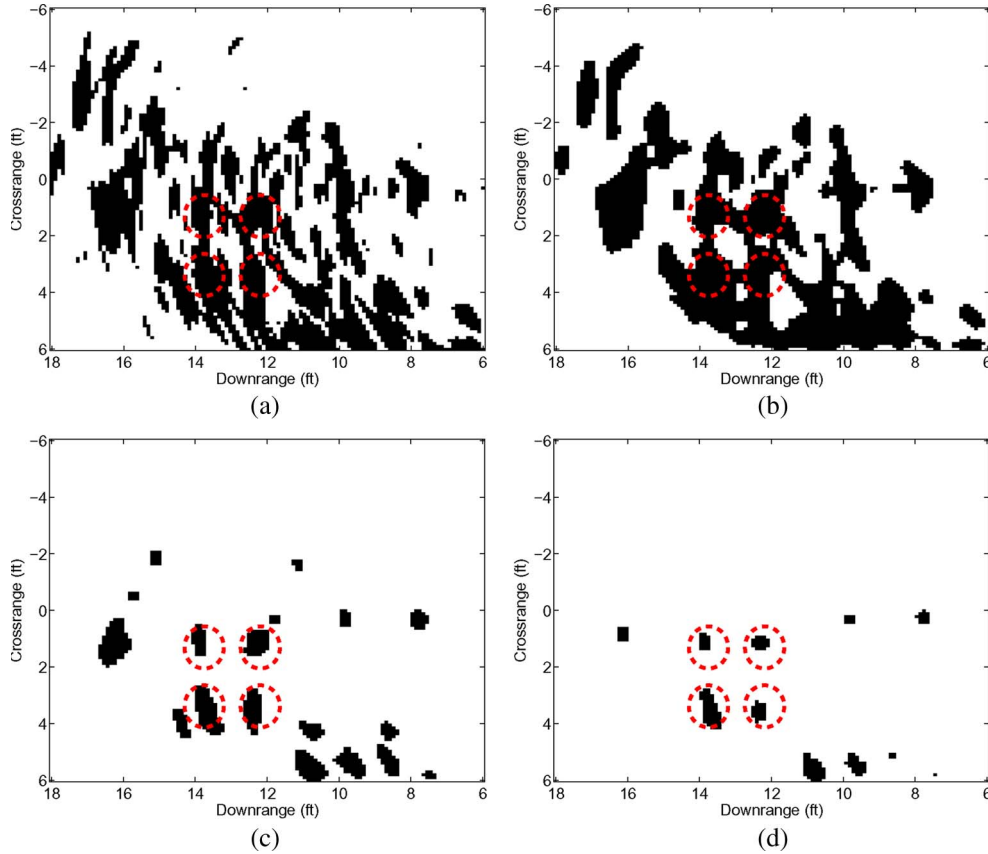


Fig. 10. Iterative detection scheme for single-view images. (a) Initialization, $F_C^{NP,I}(i,j)$, $\tilde{p}_{FA} \approx 0.26$. (b) Cleaned image, $F_C^{NP,I}(i,j)$, $\tilde{p}_{FA} \approx 0.24$. (c) Iteration 1, $\tilde{p}_{FA} \approx 0.05$. (d) Iteration 5, $\tilde{p}_{FA} \approx 0.01$.

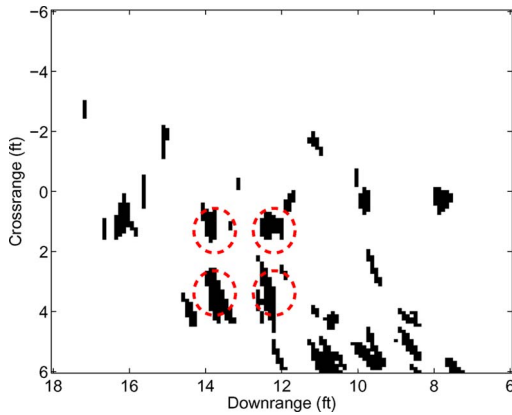


Fig. 11. Detection results using OSCFAR, $\alpha \approx 0.01$.

with $i = 1, \dots, N_x$ and $j = 1, \dots, N_y$. The image fusion result using the LRT is shown in Fig. 13(a) for a false-alarm rate of $\alpha = 0.01$. Compared with Fig. 8(b), a reduction of clutter can be observed when using two TTW radar images. Fig. 13(b) shows the resulting binary image one would obtain when using the simple multiplication scheme described in Section II-B. It can be seen that, in this specific case, the four table legs cannot be detected because strong reflections occur only in one of the TTW radar images and will thus be blanked out by simple multiplications.

The LRT allows for more flexibility, as detailed in Section II-C. The ROC for the multiview imaging scenario is

shown in Fig. 14. It is clear that, although the (dashed-dotted curve) ROC of the side-wall image is considerably worse than the (dotted curve) ROC of the front-wall image, fusion provides superior results. Additionally, the theoretical ROC for $M = 2$ is shown, which can be derived using the relation from (29).

D. 3-D Imaging

The Neyman–Pearson test, as well as the iterative approach and the OSCFAR, can easily be extended to 3-D imaging by performing the proposed detection techniques on a set of B-Scan images at different heights [21]. We consider the 3-D scene shown in Fig. 3, using the complete height from -40 in (bottom of the table) to $+20$ in (top of the dihedral) with respect to the antenna array center. Fig. 15(a) shows the 3-D detection result when using the LRT with a false-alarm rate of 1% and only considering the data measured from the front wall ($M = 1$).

The parameter set used to tune the LRT consists of the maximum-likelihood estimates obtained in Section III, Case 3) ($\hat{\mu} = 0.53$, $\hat{\sigma}_0 = 0.19$, $\hat{\sigma}_1 = 0.18$), which represent the ideal parameters for the table legs’ height. These can be seen as the average statistics of the whole 3-D scene (medium amount of clutter, still visible targets). It can be seen that the 3-D detection result is rather poor, which is due to the fact that the same statistics are used for every height of the 3-D image. Although the dihedral at height 0 in $< h < +15.5$ in is resolved

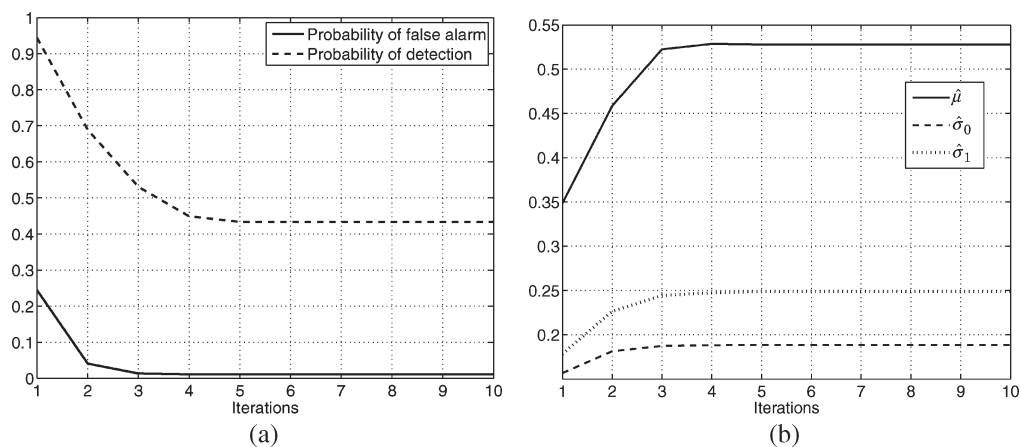


Fig. 12. Convergence of parameters using the iterative detection scheme. (a) \tilde{p}_{FA} and \tilde{p}_D . (b) $\hat{\mu}$, $\hat{\sigma}_0$, and $\hat{\sigma}_1$.

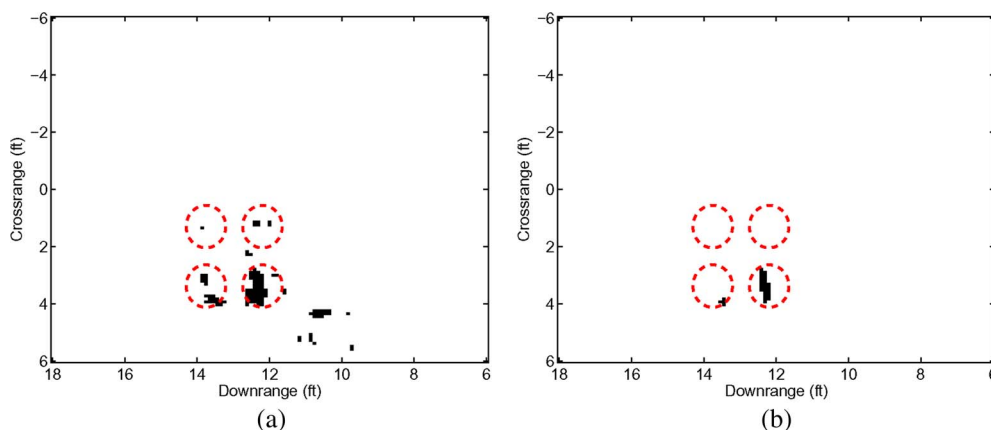


Fig. 13. Image fusion results, $\alpha = 0.01$. (a) LRT. (b) Simple multiplication.

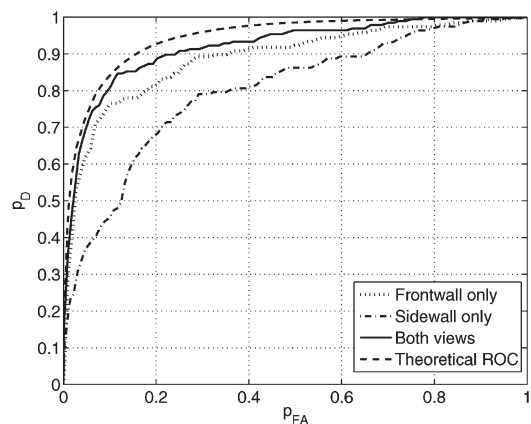


Fig. 14. ROC for multiview imaging.

(indicated by a green circle), the amount of clutter at the table’s height ($-40 < h < -20$ in, indicated by a red circle) is rather large. This coincides with the 2-D results described earlier.

When extending the LRT to $M = 2$, i.e., also considering the data measured at the side wall, the 3-D detection result is shown in Fig. 15(b). As already demonstrated for the 2-D case, the amount of clutter is reduced, and the (red circle) table response is now visible at approximately 12–14 ft downrange. The drawback, however, is that the dihedral is no longer resolved. This is due to the fact that the parameter choice for the LRT is “tuned”

to the pdfs expected at the table height. As shown in Section III, the ideal parameters for the dihedral height significantly differ from those at other heights.

The performance of the iterative approach is shown in Fig. 15(c). The main advantage of this procedure is that it adapts itself to the image statistics which vary with height. It is clear that both the (green circle) dihedral and the (red circle) table can be resolved. Further, one can observe an additional response above the table, which is due to the (yellow circle) metal sphere. This object is not shown in either Fig. 15(a) or (b). However, we also observe an increasing amount of clutter at a height $h > 0$ in. This requires further extensions of the iterative approach to better cope with highly varying image statistics.

The 3-D result when using the OSCFAR detector is shown in Fig. 15(d). As for the 2-D case, we observe an increased amount of clutter, which complicates detection. However, it shall be noted that one iteration of the proposed scheme needs approximately as much computation time as the OSCFAR, i.e., for 4–5 iterations, which was sufficient in our experiments, the iterative detection scheme needs 4–5 times more computations compared with the OSCFAR.

VII. CONCLUSION

In this paper, the target detection of objects behind walls has been considered. A Neyman–Pearson test has been derived for

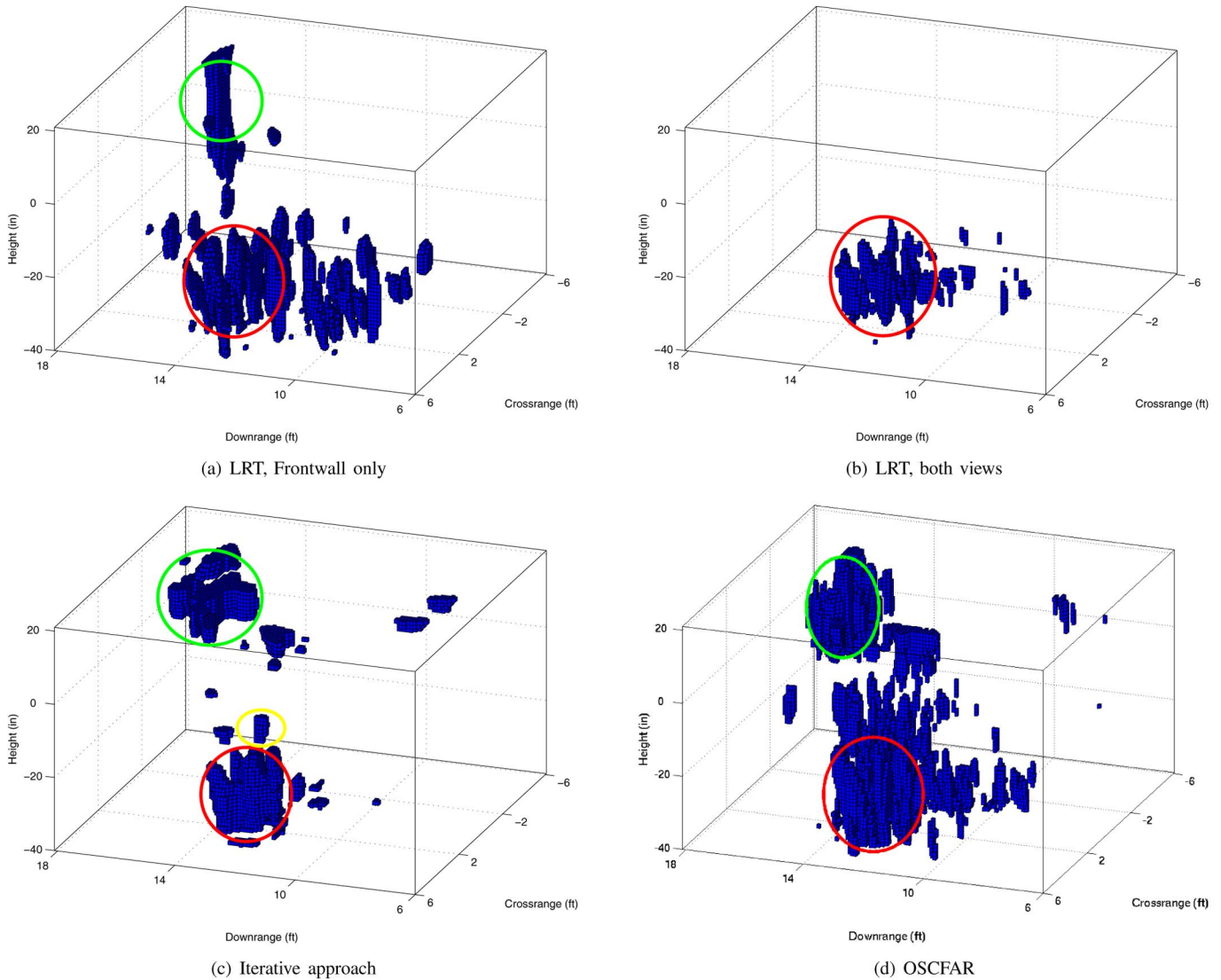


Fig. 15. Three-dimensional detection results. (a) LRT, front wall only. (b) LRT, both views. (c) Iterative approach. (d) OSCFAR.

single- and multiple-view TTW radar imaging. Experimental results have been used to motivate the use of probability density functions to describe the null and alternative hypotheses. Furthermore, the effect of wall parameter errors on these pdfs has been examined. An iterative detection scheme has been developed which adapts the detector parameters to the radar image statistics. Both detection schemes have been evaluated using real data in a semicontrolled environment. It was shown that the ROCs of the detector can be improved by using multiple vantage points for image acquisition. The proposed iterative detection scheme has shown good performance when applied to the experimental data, where the detector parameters are unknown.

REFERENCES

- [1] D. D. Ferris and N. C. Currie, "A survey of current technologies for through-the-wall surveillance (TWS)," *Proc. SPIE*, vol. 3577, pp. 62–72, Jan. 1998.
- [2] E. Baranoski, "Through wall imaging: Historical perspective and future directions," in *Proc. 33rd IEEE ICASSP*, Las Vegas, NV, 2008, pp. 5173–5176.
- [3] F. Ahmad and M. G. Amin, "Noncoherent approach to through-the-wall radar localization," *IEEE Trans. Aerosp. Electron. Syst.*, vol. 42, no. 4, pp. 1405–1419, Oct. 2006.
- [4] F. F. Ahmad, Y. Y. Zhang, and M. M. G. Amin, "Three-dimensional wideband beamforming for imaging through a single wall," *IEEE Geosci. Remote Sens. Lett.*, vol. 5, no. 2, pp. 176–179, Apr. 2003.
- [5] L.-P. Song, C. Yu, and Q. H. Liu, "Through-wall imaging (TWI) by radar: 2-D tomographic results and analyses," *IEEE Trans. Geosci. Remote Sens.*, vol. 43, no. 12, pp. 2793–2798, Dec. 2005.
- [6] S. M. Kay, *Fundamentals of Statistical Signal Processing*, vol. 2. Englewood Cliffs, NJ: Prentice-Hall, 1998.
- [7] F. Ahmad, "Multi-location wideband through-the-wall beamforming," in *Proc. 33rd IEEE ICASSP*, Las Vegas, NV, 2008, pp. 5193–5196.
- [8] F. Soldovieri, R. Solimene, and G. Prisco, "A multiarray tomographic approach for through-wall imaging," *IEEE Trans. Geosci. Remote Sens.*, vol. 46, no. 4, pp. 1192–1199, Apr. 2008.
- [9] F. Ahmad and M. G. Amin, "Wideband synthetic aperture imaging for urban sensing applications," *J. Franklin Inst.*, vol. 345, no. 6, pp. 618–639, Sep. 2008.
- [10] A. M. Zoubir and D. R. Iskander, *Bootstrap Techniques for Signal Processing*. Cambridge, U.K.: Cambridge Univ. Press, 2004.
- [11] F. Ahmad, M. G. Amin, and S. A. Kassam, "Through-the-wall wideband synthetic aperture beamformer," in *Proc. IEEE Antennas Propag. Soc. Int. Symp.*, Monterey, CA, Jun. 20–25, 2004, vol. 3, pp. 3059–3062.
- [12] B. Silverman, *Density Estimation for Statistics and Data Analysis*. London, U.K.: Chapman & Hall, 1986.

- [13] S. Papsou and R. M. Narayanan, "Multiple location SAR/ISAR image fusion for enhanced characterization of targets," *Proc. SPIE*, vol. 5788, pp. 128–139, May 2005.
- [14] G. Wang, M. G. Amin, and Y. Zhang, "New approach for target locations in the presence of wall ambiguities," *IEEE Trans. Aerosp. Electron. Syst.*, vol. 42, no. 1, pp. 301–315, Jan. 2006.
- [15] G. Wang and M. G. Amin, "Imaging through unknown walls using different standoff distances," *IEEE Trans. Signal Process.*, vol. 54, no. 10, pp. 4015–4025, Oct. 2006.
- [16] F. Ahmad, M. G. Amin, and G. Mandapati, "Autofocusing of through-the-wall radar imagery under unknown wall characteristics," *IEEE Trans. Image Process.*, vol. 16, no. 7, pp. 1785–1795, Jul. 2007.
- [17] M. Dehmollaian and K. Sarabandi, "Refocusing through building walls using synthetic aperture radar," *IEEE Trans. Geosci. Remote Sens.*, vol. 46, no. 6, pp. 1589–1599, Jun. 2008.
- [18] R. C. Gonzales and R. E. Woods, *Digital Image Processing*. Englewood Cliffs, NJ: Prentice-Hall, 2001.
- [19] H. Rohling, "Radar CFAR thresholding in clutter and multiple target situations," *IEEE Trans. Aerosp. Electron. Syst.*, vol. AES-19, no. 4, pp. 608–621, Jul. 1983.
- [20] F. Ahmad and M. G. Amin, "Through-the-wall polarimetric imaging," in *Proc. SPIE Symp. Defense Security, Algorithms Synthetic Aperture Radar Algorithms XV Conf.*, Orlando, FL, Mar. 2008, pp. 697 00N-1–697 00N-10.
- [21] R. Solimene, F. Soldovieri, G. Prisco, and R. Pierri, "Three-dimensional microwave tomography by a 2-D slice-based reconstruction algorithm," *IEEE Geosci. Remote Sens. Lett.*, vol. 4, no. 4, pp. 556–560, Oct. 2007.



Christian Debes (S'06) received the B.Sc. and M.Sc. degrees in electrical engineering from the Darmstadt University of Technology, Darmstadt, Germany, in 2004 and 2006, respectively, where he is currently working toward the Ph.D. degree in the Signal Processing Group, Institute of Telecommunications.

His research interests include detection, classification, and image processing with applications to radar imaging.



Moeness G. Amin (F'01) received the Ph.D. degree from the University of Colorado, Boulder, in 1984.

He has been a member of the faculty of Villanova University, Villanova, PA, since 1985, where he is currently a Professor with the Department of Electrical and Computer Engineering and the Director of the Center for Advanced Communications. He has over 400 publications in the areas of wireless communications, time–frequency analysis, smart antennas, interference cancellation in broadband communication platforms, direction finding,

GPS technologies, over-the-horizon radar, and radar imaging. He was the Guest Editor of the September 2008 special issue of the *Journal of Franklin Institute* (Elsevier) on advances in indoor radar imaging, and is the Co-Guest Editor of the May 2009 special issue of the IEEE TRANSACTIONS ON GEOSCIENCE AND REMOTE SENSING on remote sensing of building interior.

Dr. Amin is a Fellow of the International Society of Optical Engineering. He was a Distinguished Lecturer of the IEEE Signal Processing Society for 2003–2004. He is a member of the Franklin Institute Committee on Science and the Arts and was a member of the IEEE Signal Processing Society Technical Committee on Signal Processing for Communications during 1998–2002 and of the IEEE Signal Processing Society Technical Committee on Statistical Signal and Array Processing during 1995–1997. He was the recipient of the IEEE Third Millennium Medal; the 1997 Villanova University Outstanding Faculty Research Award; and the 1997 IEEE Philadelphia Section Service Award. He was the Cochair of the Special Sessions of the 2008 IEEE International Conference on Acoustics, Speech, and Signal Processing, Las Vegas, NV; the Technical Chair of the 2nd IEEE International Symposium on Signal Processing and Information Technology, Morocco, 2002; the General and Organization Chair of the IEEE Workshop on Statistical Signal and Array Processing, Pennsylvania, 2000; and the General and Organization Chair of the IEEE International Symposium on Time–Frequency and Time–Scale Analysis, Pennsylvania, 1994. He was an Associate Editor of the IEEE TRANSACTIONS ON SIGNAL PROCESSING during 1996–1998.



Abdelhak M. Zoubir (F'08) received the Dr.-Ing. degree from Ruhr-Universität Bochum, Bochum, Germany.

He was with the Queensland University of Technology, Brisbane, Australia, from 1992 to 1998, where he was an Associate Professor. In 1999, he was with the Curtin University of Technology, Bentley, Australia, as a Professor of telecommunications and was the Interim Head of the School of Electrical and Computer Engineering from 2001 to 2003. Since 2003, he has been with Darmstadt

University of Technology, Darmstadt, Germany, where he is currently with the Institute of Telecommunications, Darmstadt University of Technology, as a Professor and the Head of the Signal Processing Group. His research interest includes statistical methods for signal processing, with emphasis on bootstrap techniques, robust detection, and estimation and array processing applied to telecommunications, car-engine monitoring, and biomedicine. He has published extensively on these areas. He currently serves on the Editorial Boards of the European Association for Signal and Image Processing (EURASIP) journals *Signal Processing* and the *Journal on Advances in Signal Processing*.

Prof. Zoubir was the Deputy Technical Chair (Plenary and Special Sessions) of the IEEE International Conference on Acoustics, Speech, and Signal Processing (ICASSP-94), the Technical Chair of the 11th IEEE Workshop on Statistical Signal Processing, 2001, the General Cochair of the 3rd IEEE International Symposium on Signal Processing and Information Technology, and the General Cochair of the 5th IEEE Workshop on Sensor Array and Multichannel Signal Processing (SAM 2008). He was a member of the Technical Committee, as Cochair for Plenary Sessions, for ICASSP-08. He was an Associate Editor of the IEEE TRANSACTIONS ON SIGNAL PROCESSING from 1999–2005. Since 2009, he has been a member of the Senior Editorial Board of the IEEE JOURNAL ON SELECTED TOPICS IN SIGNAL PROCESSING. He is the Vice-Chair of the IEEE Signal Processing Society (SPS) Technical Committee on *Signal Processing Theory and Methods* (member from 2002 to 2007) and a member of the IEEE SPS Technical Committee on *Sensor Array and Multichannel Signal Processing* (since 2007). He was a member of the IEEE SPS Technical Committee on *Signal Processing Education* from 2006 to 2008. He is an elected member of the AdCom for EURASIP.